Accepted Manuscript

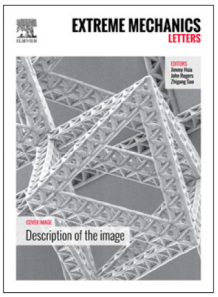

An aeroelastic flutter based triboelectric nanogenerator as a self-powered active wind speed sensor in harsh environment

Minyi Xu, Yi-Cheng Wang, Steven L. Zhang, Wenbo Ding, Jia Cheng, Xu He, Peng Zhang, Zhengjun Wang, Xinxiang Pan, Zhong Lin Wang

PII: S2352-4316(17)30078-0
DOI: http://dx.doi.org/10.1016/j.eml.2017.07.005
Reference: EML 298

To appear in: *Extreme Mechanics Letters*

Received date : 19 May 2017
Revised date : 20 July 2017
Accepted date : 21 July 2017

Please cite this article as: M. Xu, Y. Wang, S.L. Zhang, W. Ding, J. Cheng, X. He, P. Zhang, Z. Wang, X. Pan, Z.L. Wang, An aeroelastic flutter based triboelectric nanogenerator as a self-powered active wind speed sensor in harsh environment, *Extreme Mechanics Letters* (2017), http://dx.doi.org/10.1016/j.eml.2017.07.005

An aeroelastic flutter based triboelectric nanogenerator as a self-powered active wind speed sensor in harsh environment

Minyi Xu[1, 2, §], Yi-Cheng Wang[1, §], Steven L. Zhang[1, §], Wenbo Ding[1], Jia Cheng[1], Xu He[1], Peng Zhang[1], Zhengjun Wang[1], Xinxiang Pan[2], and Zhong Lin Wang[1, 3,*]

[1] School of Materials Science and Engineering, Georgia Institute of Technology, Atlanta, Georgia 30332-0245, United States

[2] Marine Engineering College, Dalian Maritime University, Dalian, 116026, China

[3] Beijing Institute of Nanoenergy and Nanosystems, Chinese Academy of Sciences, Beijing 100085, China

Abstract

With the development of internet of things and sensor networks, self-powered sensors are highly desirable. In this study, we present a simple but practical design of an aeroelastic flutter based triboelectric nanogenerator (AF-TENG) that could harvest energy from wind and serve as an active wind speed sensor. The fabricated AF-TENG consists of two copper layers and a membrane in a cuboid acrylic channel. The effect of membrane materials, including fluorinated ethylene propylene (FEP), polytetrafluoroethylene (PTFE) and Kapton (PI), length of membrane, inlet wind speed and humidity on the performance of AF-TENG have been systematically investigated. As wind flows through a designed channel, the membrane moves up and down between copper surfaces periodically, which results in a periodic electrical output signals of the AF-TENG. The corresponding frequency of the AF-TENG signal is found to increase in a robust linear relationship with the wind speed. Interestingly, as environmental humidity increases, the amplitude of voltage and current output of the AF-TENG deceases dramatically, while the frequency of the output remains the same due to high humidity can decrease the charge density in the membrane surface but have no effect on the fluttering motion of the membrane. The real-time wind speed measured through analyzing frequency of the voltage of the AF-TENG agrees well with a commercial wind speed sensor, and the corresponding speed sensitivity is about 0.13 (m/s)/Hz or 7.7 Hz/(m/s). Therefore, the fabricated self-powered AF-TENG has shown potential applications in wireless environmental monitoring networks, even in high humidity environment.

Keywords: triboelectric nanogenerator; fluid dynamics; self-powered sensor; wind energy; harsh environment

1. Introduction

Self-powered system is a promising concept for the realization of environmental wireless sensor networks. Due to the enormous demands of distributed nodes in the networks, the disadvantages of conventional battery-based sensors, such as large package size, low device maintainability, high system cost, limited lifetime and risk of environment pollution, are important issues [1, 2]. Thus, a battery-free autonomous system that scavenges its operation energy from the surroundings is highly desired. Recently, TENG is found to produce electricity by using the Maxwell's displacement current, which is significant for fabricating more effective TENGs and their commercial products [3]. Since TENG can generate electrical signals from many types of mechanical motions in the natural environment, it can serve as a self-powered active sensor [3-13]s.

Flow-induced vibration is known as an attractive source of energy harvesting, because of its ubiquity in the environment and non-complex structure for trapping it [14, 15]. Recently, the interaction of a flag and a rigid plate as a powerful vibration source for triboelectric nanogenerator have attracted much attention [7, 16-23]. However, most of these previous work just used the flutter driven TENG to harvest wind energy at high critical wind speed (>6 m/s) at which the membrane in the TENG begins to flutter. This limits the potential applications of such TENG, due to the global average wind speed at 10 m height over land was 3.28 m/s [24]. The average output power density depends on contact force, effective contact area and types of contact motion, and an average output power of approximately 0.86 mW was found at a wind speed of 15m/s [7]. Even though a linear relationship between the average output current peak and the wind speed can be obtained[20], the sensitivity of their TENG device is only 0.09 μA/(m/s). In addition, the electrical output of TENG is found to be influenced by high humidity, hysteresis effect [25] and electrostatic discharge phenomenon [26].Thus, new approaches are needed to improve the sensitivity and critical wind speed of TENG-based wind speed sensor.

There is considerable amount of research on the basic dynamics of flexible flags, which can be bent, folded, twisted or waved with flow of the wind [27-30]. The first experimental study on fluttering behavior was performed by Taneda [31] with a flag made of various fabrics and shapes. In addition, using one-dimensional filaments, the distinct dynamic states (for example, a stretched straight state and a fluttering state) and the coupled interaction between the states were observed through a flowing soap membrane experiment [32]. Interestingly, Shelley et al.[33] showed that the fluttering frequency f of a flag was proportional to the flow speed. The resultant non-dimensional frequency parameter, i.e. Strouhal number ($St = fL/U$) is approximately 1.2, where L is the flag length, U is incoming fluid speed, while the Strouhal number based on fluttering amplitude increases with flow speed between

0.22 and 0.3. Thus, the relationship between the frequency and wind speed, or between Strouhal number and Reynolds number (Re = UL/ν with ν being the fluid kinematic viscosity) for a fluttering membrane can be used to calculate the flow velocity by measuring the fluttering frequency.

In the present work, we present a simple but practical design for an aeroelastic flutter based TENG (AF-TENG) that could serve as an active wind speed sensor by measuring the fluttering frequency instead of measuring the output voltage/current. The fabricated AF-TENG consists of two copper layers and another membrane in a cuboid acrylic channel. The inner side of both top and bottom surface of the wind channel were coated with Copper layer of thickness ~ 100 nm by a RF magnetron sputtering system. The effects of different membrane materials, including fluorinated ethylene propylene (FEP), polytetrafluoroethylene (PTFE) and Kapton, length of membrane, inlet wind velocity and humidity on the performance of AF-TENG have been systematically investigated. A theoretical analysis to show the mechanism of the membrane motion due to the wind flow is also proposed. Our fabricated self-powered AF-TENG has shown potential applications in wireless environmental monitoring networks, even in high humidity environment, where previous reports of self-powered wind sensors could not achieve.

2. Methods

2.1 Fabrication of the aeroelastic flutter driven TENG

The FEP, Kapton, and PTFE thin films with thicknesses of 25.4 μm and 50.8 μm were purchased from McMaster and used. A channel with dimension of 2 cm (width) × 2 cm (height) × 10 cm (length) was made of acrylic. The inner side of both top and bottom surface of the wind channel were coated with Copper layer of thickness ~ 100 nm by a RF magnetron sputtering system (PVD 75, Kurt. J. Lesker Company). The two Copper layers are serving as the two electrodes. Finally, the membrane (FEP, Kapton, or PTFE) was fixed in the middle plane of the wind channel.

2.2 Measurement of the fabricated devices

In the wind tunnel system, a specific holder was attached to install the AF-TENG. Both the top and bottom electrodes were connected to the Keithley 6514 electrometer to measure the electrical performances including the open-circuit voltage, short-circuit current and transferred charge. The fluttering behavior of the membrane was characterized by capturing the average fluttering motions using the camera (Cannon 5D Mark III). A commercial humidifier (TaoTronics Ultrasonic Humidifiers) was used to increase the humidity in the wind channel. For the self-powered wind speed

system, a homemade data acquisition system was used to record the output voltage signals in real time.

3. Results and discussion

3.1 Structure and fluttering behavior of AF-TENG

As shown in **Fig. 1 (a)**, for the fabrication of AF-TENG, a flexible membrane was placed in the middle of a rigid channel with the size of 2 cm (width W) × 2 cm (height H) × 12 cm (length L_C). Both the top and bottom surfaces of the channel were coated with copper layer of thickness ~ 100 nm by a RF magnetron sputtering system, serving as the two electrodes. In order to generate electricity from low wind speeds, three membrane materials with the highest electron affinity, i.e., FEP, Kapton, and PTFE were studied systematically. A homemade wind tunnel was built by acrylic to produce the uniform wind speed. The incoming wind speed (U) in the experimental section ranges from 0 to 10.8 m/s, which includes the global average wind speed [24].

To optimize the electrical output of the AF-TENG, it is important to understand the flutter behavior of the membrane in a rigid channel. Assuming that the deformation of the membrane is two-dimensional, and the viscoelastic damping of the material and the viscous boundary layers are negligible, the Euler-Bernoulli beam theory [7, 23, 34-36], which applies to thin membrane such as our membrane, provides a dimensionless equation (1) to model the motion of the fluttering membrane,

$$\frac{\partial^2 V^*}{\partial T^{*2}} + \frac{1}{U^*}\frac{\partial^4 V^*}{\partial X^{*4}} = M^* \left\langle \Delta P^* \right\rangle_z \qquad (1)$$

Here, V^*(= V/L) denotes the dimensionless transverse displacements of the membrane at a given dimensionless horizontal coordinate X^* (= X/L), and dimensionless time T^* (= TU/L). ΔP^* (= $\Delta P/\rho_a U^2$) is the dimensionless pressure difference between the lower and upper surface of the membrane. $\langle . \rangle_Z$ denotes the average along the spanwise direction. The air density ρ_a=1.204 kg/m^3 at atmospheric pressure and 23 □. V, X, T and ΔP are transverse displacements, streamwise coordinate, time and pressure difference, respectively. $M^* = \rho_a L/\rho h$ is fluid-solid mass ratio with h is the membrane thickness and ρ_a, ρ stand for mass density of air and membrane. $U^* = UL(\rho L/D)^{1/2}$ denotes the non-dimensional velocity, i.e., where U is the incoming wind speed, and D is the flexural rigidity of the membrane and is deduced as $D = Eh^3/(12(1-v^2)^{1/2})$ with E being Young's modulus (tensile elastic modulus), v being Poisson's ratio [23, 37]. Usually, from the equation, the flutter behavior of the two-dimensional membrane are

described using fluid-solid mass ratio M^* and non-dimensional velocity U^* due to the stability boundary of the fluttering membrane can be characterized by the two parameters [7]. Detailed physical dimensions and mechanical properties of the experimental membranes are listed in the **Supplementary Table S1**.

It is worth to note that, in present study, the membrane is confined in a rigid channel. The intermittent contacts, electrostatic interactions between the membrane and the electrodes are boundary conditions that are difficult to define for modeling using equation (1). To further discuss the motion of fluttering membrane, previous studies have proposed a particular solution of Euler-Bernoulli beam theory by using a travelling harmonic wave combined with a spatially varying envelope [23, 32],

$$V^*(X^*,T^*) = A^*(X^*)\sin(2\pi(StT^*+X^*/\lambda^*)) \qquad (2)$$

where A^* ($= A/L$) is the dimensionless spatial envelope function, λ^* ($= \lambda/L$) is the dimensionless reduced wavelength and St ($= fL/U$) is the dimensionless fluttering frequency, i.e. Strouhal number. A, λ and f are spatial envelope function, wavelength and fluttering frequency, respectively. Although this simplification was initially for free fluttering membranes, it is interesting to find that the present fluttering membrane in a rigid channel can be also represented by a simple travelling harmonic wave combined with a spatially varying envelope, see **Fig. 1b**. This is also observed and valid in the work of Perez et al.[23]. Therefore, the membrane moving up and down periodically driven by wind flow can result in periodical electrical output signals (voltage, current, charge) and thus the fluttering frequency is equivalent to the electric output signals frequency. By utilizing the electrical signal frequency and the Strouhals number, one can then calculate the wind speed directly. This is discussed in detail in Section 3.3.

Figure 1b shows the fluttering behavior of FEP, Kapton and PTFE in the rigid channel at wind speed of 10m/s. The length and width of these membranes are 10 cm. and 1.8 cm, respectively. It is obvious to find that the difference in dimensions (length L, width w and thickness t), fluid-mass ratio and flexural rigidity of the FEP, Kapton and PTFE membranes, resulted in different fluttering behavior. For a given length and width, the average contact area between the thick FEP membrane (54.8μm) and rigid plate increases about 20% compared to that of thinner FEP membrane (25.4μm). In addition, among the FEP, Kapton and PTFE with the same thickness of 54.8μm, the FEP has the largest contact area, while the contact area between Kapton and the rigid plate is the smallest. This may be due to the largest flexural rigidity of the Kapton, see Table S1. Also, the contact area of the thin FEP membrane increases as the membrane length increases, and the contact area is nearly independent of the incoming wind speed for U>4.5m/s, shown in **Figure S1**.

The critical flutter speed U_{cf}, above which the flexible membrane begins

fluttering due to the destabilizing effects of inertia [7], also varies with the fluid-solid mass ratio M^* and types of the membranes. For a given thickness and density of the membrane, the increment of fluid-solid mass ratio M^* is corresponding to that of length L increment. As shown in **Fig. 1 (c**), the critical flutter velocity U_{cf} decreases quickly with increasing the fluid-solid mass ratio M^* of the membranes for $M^*<0.5$. For $M^*>0.5$, the critical flutter velocity U_{cf} of PTFE and Kapton membrane decreases slightly, while the value of U_{cf} for FEP membranes is nearly constant. It is worth to notice that the flexural rigidity of FEP membranes is smaller than those of PTFE and Kapton, shown in **Table S1**. This suggests that the membrane begins to flutter at a lower critical velocity for with increasing fluid-solid mass ratio M^* or length of membrane for a given width and thickness. With further increasing the mass ratio M^* or length of membrane, the critical flutter velocity is nearly independent of the two parameters for the membrane that has smaller flexural rigidity. Such phenomenon is also observed in Refs. [7, 23]. In addition, Figure 1(c) also shows that the critical velocity curves of PTFE and Kapton membrane are higher than that of both thick and thinner FEP membrane. This suggests that the FEP membrane begins to flutter at lower wind speed, compared the PTEF and Kapton membrane. For example, the values of U_{cf} for the PTFE, Kapton, thick and thinner FEP membranes at $M^*\approx1.4$ are 4.8 m/s, 5.0 m/s, 3.1 m/s and 2.5 m/s, respectively. This trend consists with their flexural rigidity, as shown in **Table S1**. The abovementioned experimental result is new and important, because it serves as a guideline of the membrane material and length selection for energy harvesting from a certain wind speed range.

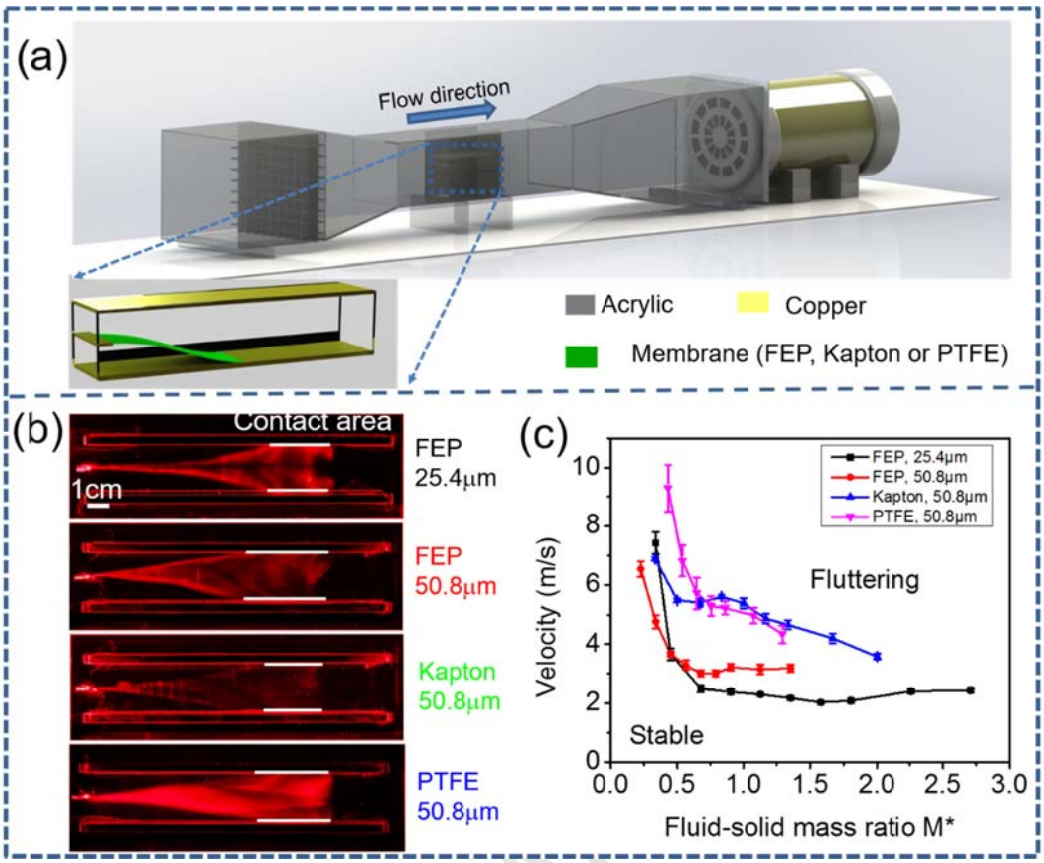

Figure 1. Experimental set-up and characterization of fluttering behavior of AF-TENG. (a) Schematic of a wind tunnel and the structural design of AF-TENG with acrylic tube size of 2 cm×2 cm×10 cm (inset); (b) Fluttering images of FEP, Kapton and PTFE with L = 10 cm, w = 1.8 cm and U = 10 m/s by a high speed camera, the white bars show the actual contact area between the membrane and the top/bottom surface; (c) The relationship between critical flutter velocity U_{cf} and the fluid-solid mass ratio M* of FEP, Kapton and PTFE membranes. Each curve separates the "stable" (without fluttering) from the fluttering regions of the membrane.

3.2 Working principle of AF-TENG

The electric generation mechanism of the AF-TENG is based on the coupling of contact triboelectrification and electrostatic induction, as depicted in **Figure 2 (a)-(b).** If the wind flow enters into the channel above a minimum speed of U_{cf}, the membrane moves up and down periodically due to the fluttering effects. When the membrane contacts the top or bottom copper surface, negative charges would be transferred from the copper to the membrane due to triboelectrification, leaving the copper as positively charged, as shown in **Fig. 2 (a).** The produced negative charges in this process can be preserved on the top and bottom membrane surface due to the nature of the dielectric material. It is worth to note that only contact area of the membrane are charged. The value of the negative charges of the FEP membrane is constant, which is

equivalent to the total positive charges of the two electrodes for a certain wind speed. However, the charges flow form one electrode to the other electrode with the external circuit when the FEP membrane moves.

To better understand the voltage distribution related to the output performance of the TENG, we only simulated the voltage distribution of the electrodes by setting charge density of the electrodes using COMSOL multiphysics software. The similar simulations are also used in many previous studies, such as [38, 39]. When the membrane moves up, i.e. separates from the bottom layer, the potential difference between the top and bottom copper layer also increases, see **Fig. 2 (b**), which demonstrates the potential distribution for three states of the A**F**-TENG under open-circuit condition. Thus, the electrons move from the top copper layer to the bottom one until the membrane contacts the top layer. Then, the membrane moves down, which makes the moving of electrons from bottom copper layer to the upper one. Thus, a periodical current signal is produced due to the periodic transfer of electrons between bottom and top copper layer, see **Fig. 2 (a)**. In addition, it is worth to note that the frequency of the electrical output signals, i.e., current, voltage and charge, is equivalent to that of membrane fluttering. This simple mechanism can be successfully employed for converting the kinematic energy of the wind into electrical energy and this device could be used for sensing the wind speed.

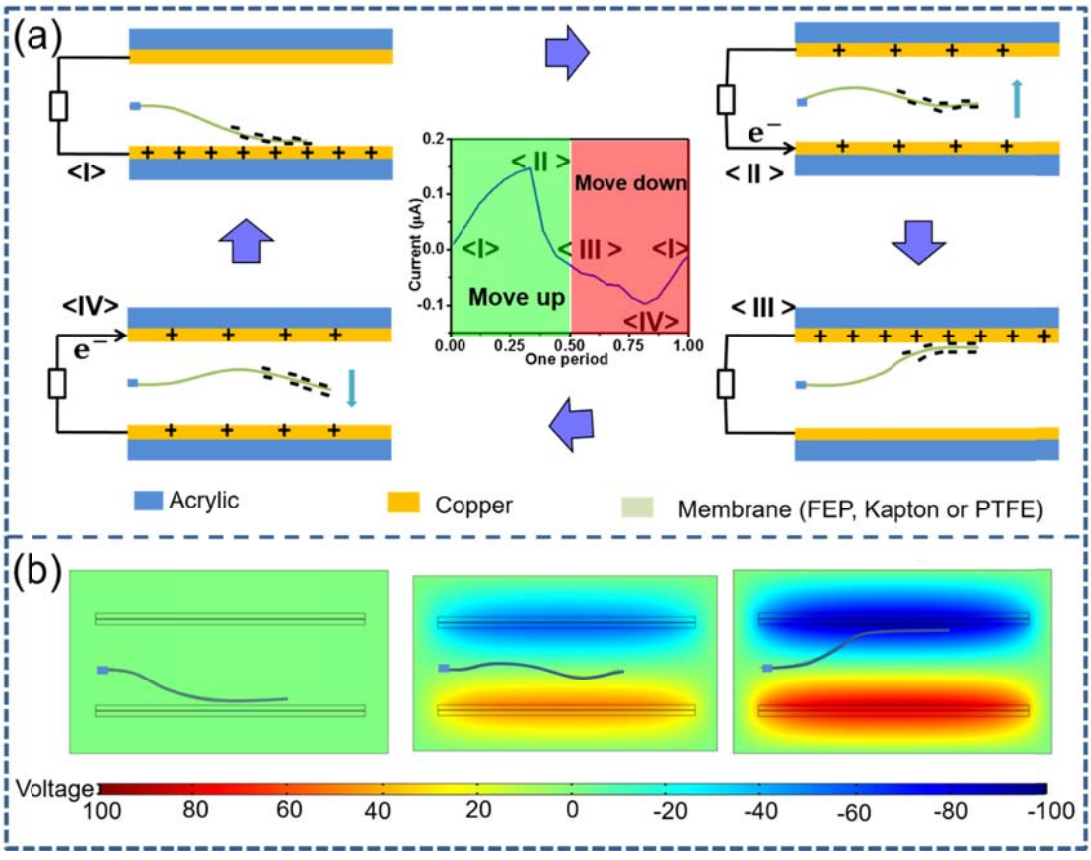

Figure 2. Mechanism of the AF-TENG. (a) Illustration of the eletricity generation process in fully cycle under wind-induced flutter of the membrane between copper plated on top and bottom of the acrylic tube. The typical current output of the AF-TENG in one period is shown as the inset. (b) COMSOL simulation of potential distribution of AF-TENG.

3.3 Performance of AF-TENG

Figure 3 shows the electrical characteristics of AF-TENG with different membrane materials, i.e., FEP, Kapton and PTFE, corresponding to same length L= 10 cm, width w=1.8 cm, and wind speed U=10 m/s. Overall, the electrical performance of those membrane directly depends on their electron affinity, contact area and fluttering frequency. The last two parameters relate to the mechanical properties, e.g., fluid-solid mass ratio, flexural rigidity and incoming wind speed. Therefore, the voltage, current and charge output of those membrane performs differently. As shown in **Fig. 3**, the PTFE membrane has the larger voltage output (60 V) compared to that of Kapton, due to its higher electron affinity and larger contact area, while the current output of the Kapton approaches to that of PTFE, due to the fluttering frequency of Kapton (46 Hz) is larger than that of PTFE (33 Hz). Similarly, compared to the thick FEP, the thinner FEP has a smaller voltage output but flutters at higher frequency (50 Hz), resulting in its current output being close to that of the thick FEP.

It is also important to note that abrupt and intermittent output declines are observed in AF-TENG, especially for the thinner FEP membrane, as shown in **Fig. 3**. The reason could be due to the loss of surface charges, which probably relates to an electrostatic discharge phenomenon between two contact pairs. This is consistent with the results in a novel asymmetrical TENG investigated by Su et al. [26]. They found three necessary premises for electrostatic discharge in TENG: the asymmetrical structure, the proper soft/rigid contact pair, and the enough thickness of the soft layer. For our case, the membrane and acrylic coated with copper forms a soft/rigid contact pair, and the small contact area and large copper layer forms an asymmetrical structure. In addition, it is found that the electrostatic discharge phenomenon is more obvious for thinner FEP membrane (25.4 μm) than the thick FEP membrane (50.8 μm). Although they flutter at the same wind speed, the fluttering frequency of the thinner FEP is 38% larger than that of the thick FEP membrane. Also, we can see that the electrostatic discharge phenomenon is obvious for FEP membrane at large wind speed, corresponding to large fluttering frequency, see **Fig. 4(d) and 5(d)**. This suggests that the contact frequency between the soft/rigid contact pair plays more important role in electrostatic discharge phenomenon, compare to the thickness of the soft membrane.

Interestingly, the fluttering frequency calculated from the electrical signals using fast Fourier transform (FFT) are quite stable, although the abrupt and intermittent electrical output declines, see **Figure 3**. This also supports that the frequency should be a more proper parameter rather than the average voltage output peak, to sense the wind velocity, as the voltage could vary by electrostatic discharge phenomena, which is of great importance in a self-powered sensing system [5].

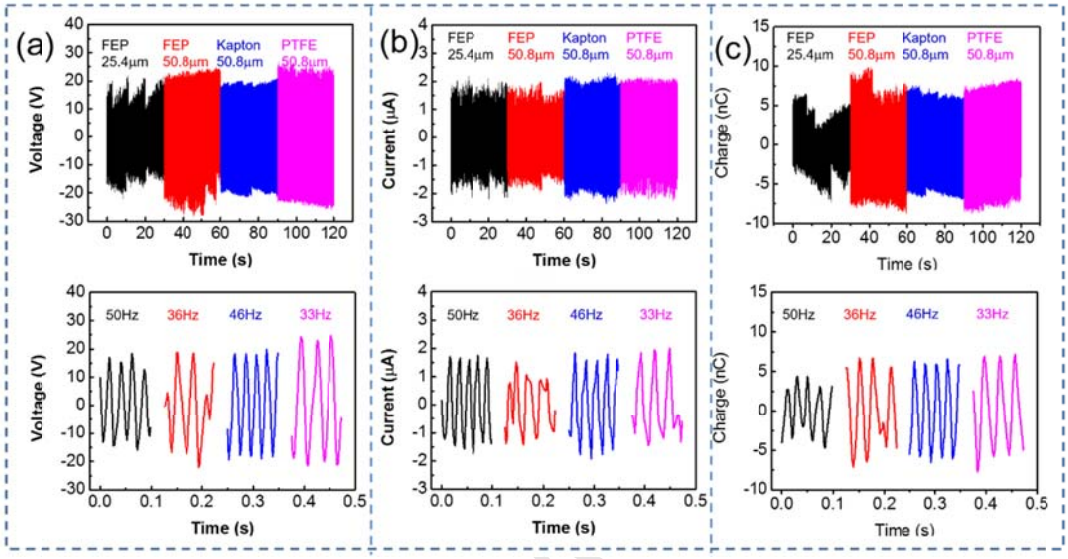

Figure 3. Electrical characteristics of AF-TENG made of FEP, Kapton or PTFE membrane with the same length L= 10 cm, width w=1.8 cm, and incoming wind velocity U=10 m/s. (a) voltage, (b) current, (c) charge. Note that, the signals shown in up figures is with time of 30 seconds, while the signals shown in down figures is with time of 0.1 second.

Figure 4 shows electrical characteristics of AF-TENG corresponding to different membrane length and incoming wind speed. To study the effect of the FEP length on the electrical output, we measured the voltage, current and charge signals for L= 3 cm, 6 cm and 10 cm at incoming wind speed U = 3.1 m/s, as shown in **Fig. 4 (a)-(c).** It is found that the amplitude of electrical signals increases as the L increases, which consisted with the increment of contact area on the increase of the FEP length, as shown in **Figure S1**. As shown in Niu et al [40], the voltage at open circuit condition V_{OC} for a single electrode TENG is proportional to the contact area S and charge density σ, i.e., $V_{OC} \sim \sigma S$. Thus, with a higher contact area due to the increase of the FEP length would result in a higher Voc. In addition, all the electrical signals are quite periodic and the fluttering frequency of the FEP corresponding to L=3 cm is the largest. Thus, we investigated the performance of the FEP corresponding to L=3 cm in detailed, due to large fluttering frequency can enhance the sensitivity of wind speed sensor.

Figure 4 (d)-(f) shows voltage, current and charge of length corresponding to

L=3cm with incoming wind speed increasing from 3.1 m/s to 10.8 m/s. When the incoming wind speed increases from 3.1 m/s to 9.2 m/s, the average voltage peak increases from 3V to 6V, then the average peak decrease from 6 V to 4.5 V with increasing wind speed from 9.2 m /s to 10.8 m/s, see **Fig. 4 (d)** and **Fig. 5 (a)**. This is consistent with the variation of average peak charge with the incoming wind speed. As the wind speed increases, the contact force between the fluttering membrane and electrode also increase. Due to the high contact force, there would be high surface charge density [41]. This would cause an increase in the *V*oc initially. For higher wind speed (>9.2 m/s), the charge density on the fluttering membrane would reach a saturated state, which is also observed in the literature [41]. However, it is important to note that abrupt and intermittent output declines are observed in AF-TENG for higher wind speed, see **Figure 4(d)-4(f).** The reason is caused by the electrostatic discharge phenomenon between two asymmetrical contact pairs [25]. Thus the loss charge on the membrane surface cause *V*oc to decrease a little in higher wind speed. For the current signals, the average current peak seems to approach an asymptotic state when the incoming wind speed exceeds 9.2 m/s. However, with increasing the length of the membrane, the average current peak increases with incoming wind speed, see **Figure S2 and S3**. The similar phenomenon was also observed by Yang et al. [20] and they proposed to use the relationship between average current peak and the wind speed as an wind speed sensor. However, it is worth to point that the observed nonlinear relation between the average current peak and the wind speed will decrease the accuracy and sensitivity of the wind speed sensor.

Figure 4 (g)-(i) shows voltage, current and charge of length *L*=3 cm with incoming wind speed decreasing from the 10.8 m/s to 3.1 m/s. The presented electrical output at low velocity range of 3.1 m/s ~ 9.2 m/s become larger, compared to those measured with increasing wind speed. For example, the voltage output peak at 3.1m/s increases from 3 V to 10 V. The reason is that the tribocharge on the surface of FEP membrane generating at the high incoming wind speed (10.8 m/s) do not immediately disappear but gradually decay over a period of hours. Therefore, the output measured at low wind seed followed immediately after a high speed wind results in enhanced output performance, **see Fig. 5(a)-(c)**. This is consistent with the study of hysteretic behavior of contact force response in TENG [25]. The hysteretic behavior is useful for wind energy harvesting, due to the remaining charge generated at high wind speed can make the AF-TENG obtain additional energy gain at low wind speed. However, such hysteretic behavior would influence sensitivity of TENG sensor if the relationship between current output peak and wind speed is applied [20]. Thus, it is of great importance to find a stable relationship between electrical characteristics of AF-TENG and wind speed.

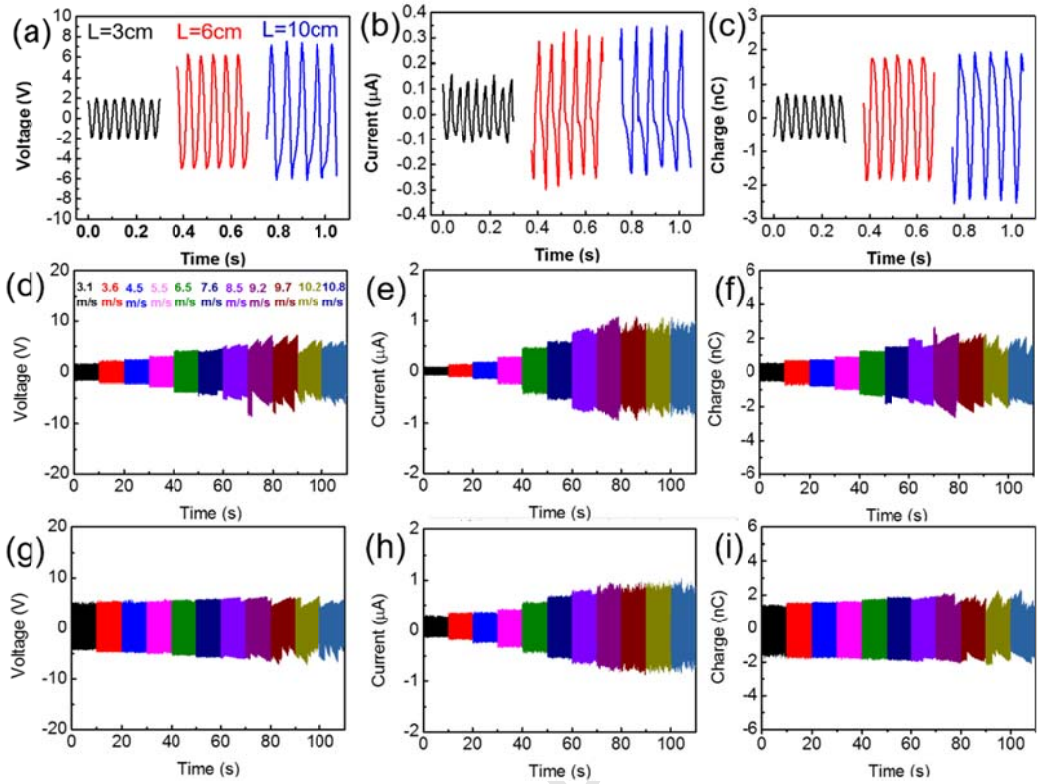

Figure 4 Electrical characteristics of AF-TENG with different length of the FEP membranes and incoming wind speed. (a) Output voltage, (b) current, (c) charge of length L=3 cm, L=6 cm, and L=10 cm for U=3.1 m/s. (d) Voltage, (e) current, (f) charge of length corresponding to L=3 cm with wind velocity increasing from 3.1 m/s to 10.8 m/s. (g) Voltage, (h) current, (i) charge of length L=3cm with velocity decreasing from 10.8 m/s to 3.1 m/s.

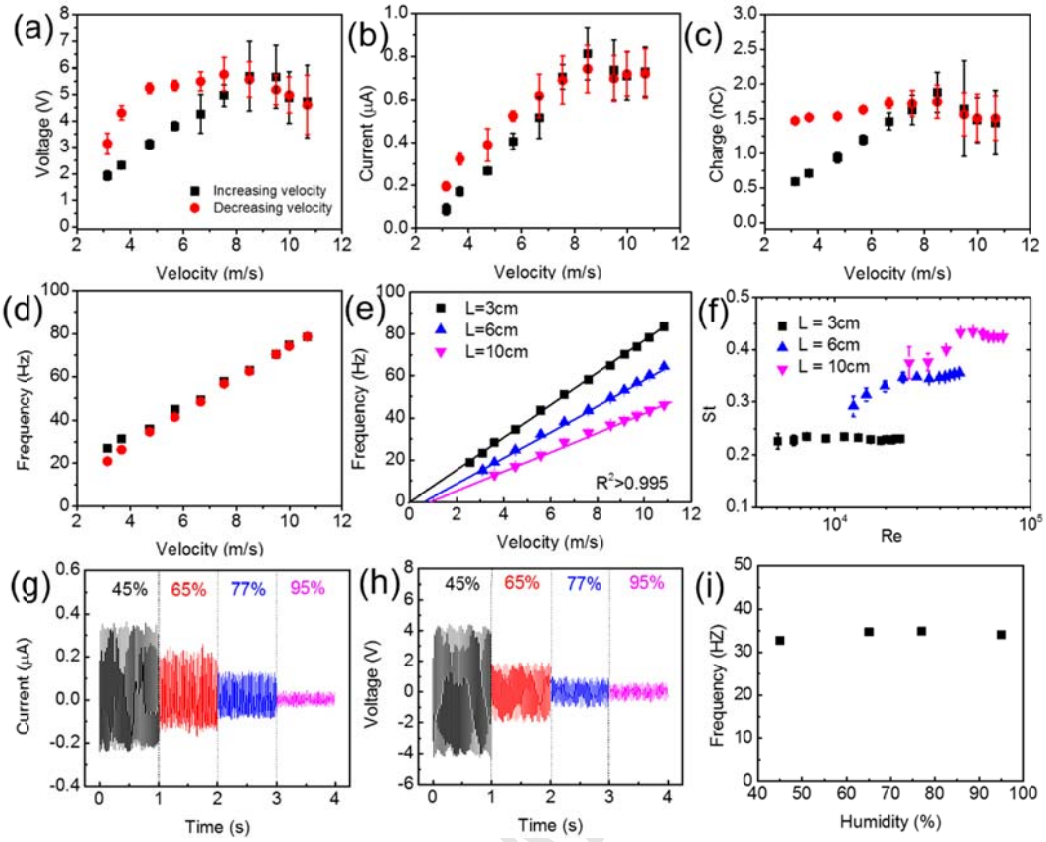

Figure 5 Hysteretic effect and humidity effect on performance of TENG. (a) Peak voltage, (b) peak current, (c) peak charge, and (d) frequency of increasing wind speed (black) and decreasing wind speed (red). (e) Frequency corresponding to velocity, and (f) Strouhal number corresponding to Reynolds number for different length. (g) Current, (h) voltage, and (i) frequency with respect to relative humidity.

Figure 5(d) shows the fluttering frequencies of FEP membrane, which are obtained by performing the fast Fourier transform (FFT) of electric signals. Interestingly, the frequency and wind speed form a linear relationship, compared to the large variation of the relationships between electrical signals, i.e., voltage, current and charge, and the incoming wind speed (**Fig. 5(a)-(c)**). Also, the frequency does not change with previous charges on the surface of the FEP, unlike that of average current peaks, see **Fig. 5(b) and 5(d)**. Moreover, **Figure 5(e)** shows the dependence of the relationship between the fluttering frequency and the incoming wind speed on the membrane length L. Here, all the relationships is highly linear, due to the corresponding R^2 for all the fitting is larger than 0.995. With increasing L = 3 cm to 10 cm, the corresponding slope of the linear relationship decreases from 7.67 to 4.71, indicating the shorter membrane length has the better speed sensitivity. For present study, the wind speed sensitivity for the FEP membrane corresponding to L = 3cm is 0.13(m/s)/Hz or 7.7Hz/(m/s).

Furthermore, the non-dimensional frequency parameter, i.e., Strouhal number as function of the Reynolds number *Re* (=*UL*/ν) is presented **in Fig. 5(f)**. In fact, two length scales can be used to define the Strouhal number: the membrane length *L* or the fluttering amplitude *A* measured as the average fluttering span [30]. For the present membranes confined in a rigid channel, their fluttering amplitude *A* is constant, i.e., the height of the channel. Therefore, the Strouhal number based on length *L* is defined as *St* (=*fL*/*U*). Here, *f* is the fluttering frequency of a membrane, which is equivalent to the frequency of output electrical signals (voltage, current, charge). The ν is the kinematic viscosity of wind, which is around 1.5×10^{-5} m^2/s at 20°C. As shown in **Fig. 5(f)**, the value of *St* is nearly constant (0.23) for the FEP membrane corresponding to *L* = 3cm as the Reynolds number increases, which is close to that of 0.22 ~ 0.31 in the experimental observation in Shelley et al.[33] and numerical investigation in Huang et al. [30]. It is worth to note that the membrane flutters in a large area without a confinement by a small channel, studied by Shelley et al.[33] and Huang et al. [30]. The lack of variation in *St* with the Reynolds number indicates that the membrane inertia dominates over the viscous force exerted on the membrane by the surrounding fluid [30]. For the longer FEP membrane (e.g., *L* = 6 cm and 10 cm), *St* increases slightly with Re increasing, and then reach a stable value of 0.35 and 0.44, respectively, after a critical Reynolds number. This is consistent with the variation of Strouhal number of vortex shedding from a circular cylinder with Reynolds number. Its Strouhal number ranges from 0.12 to 0.2 with increasing Reynolds number when periodic vortex shedding is established, and converges to about 0.2 after three dimensional shedding modes are formed [42].

In addition, the effect of relative humidity of AF-TENG performance was investigated by varying the relative humidity from 45% to 95%. Compared to that measured at humidity of 45%, the current and voltage output decreased by nearly 90% at humidity of 95%, due to the charge density on the membrane surface decreases dramatically at high humidity, as shown in **Fig. 5(g)** and **(h)**. However, humidity has no effect on fluttering motion of the membrane, thus the corresponding fluttering frequency is independent to humidity, see **Fig. 5(i).** Such finding proves that the fluttering frequency is a much more proper value to be used as the key parameter to detect the wind speed rather than average current output peaks used in previous study [20]. Also, the results demonstrated that the fabricated self-powered AF-TENG wind velocity sensor can work well in high humidity environment.

3.4 Demonstration

To test the performance of the AF-TENG as a wind speed sensor, the real-time speed of the AF-TENG and a commercial hot-wire anemometer (Testo 405i) were compared, as shown in Fig. 6a. The real-time frequency *f* is obtained from the real-time voltage output of the AF-TENG with *L*=3cm using short-time FFT, see Fig.

6b. Then, the wind speed U is obtained using the relationship between the frequency of the electrical signals e.g., voltage, and incoming wind speed, i.e., U=0.13f. The wind speed obtained by both AF-TENG and the hotwire anemometer agrees well, as shown in Fig. 6(c) and Supplementary Movie 1 for both increasing wind velocity and decreasing velocity. (Explain link to Figure 1c)

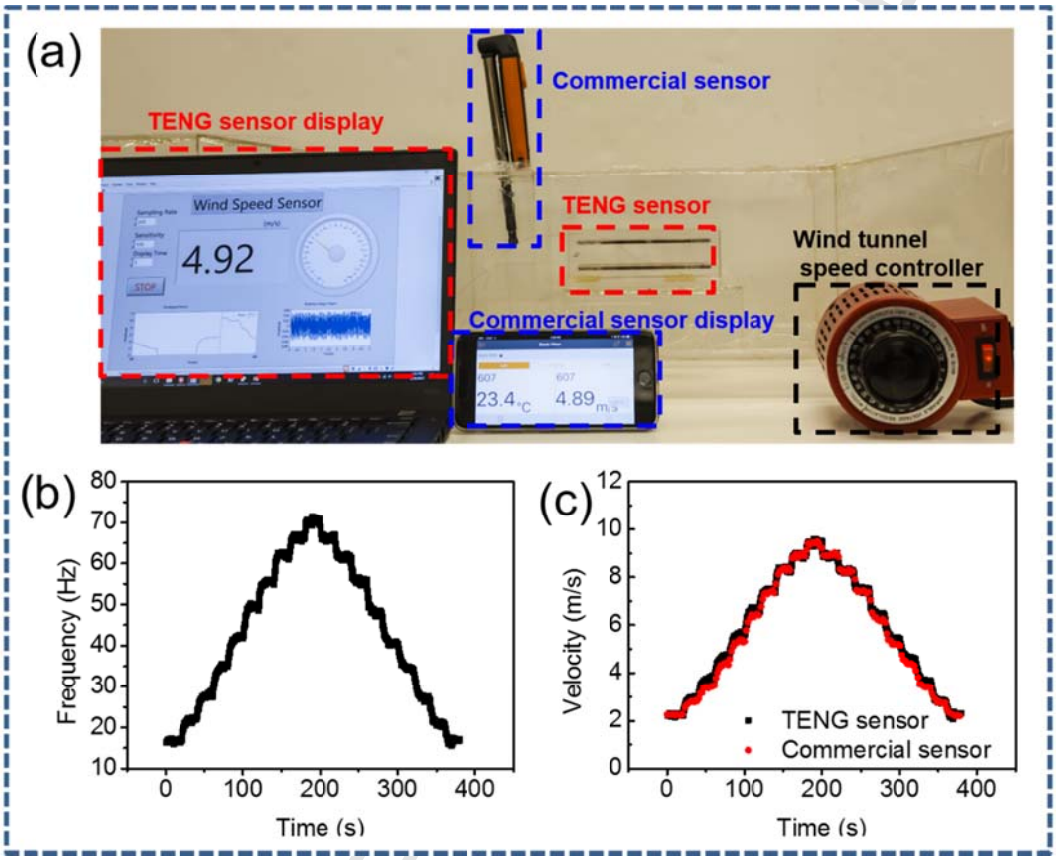

Figure 6. Application of AF-TENG wind speed sensor for obtaining real-time velocity. (a) Photos of the real time velocity measurement using AF-TENG sensor and a commercial sensor .(b) short FFT frequency vs time, (c) Comparison of AF-TENG wind speed sensor and commercial wind speed sensor.

4. Conclusions

In summary, we presented a simple, but practical design for an aeroelastic flutter driven TENG (AF-TENG) that could harvest energy from wind and serve as an active wind speed sensor. The fabricated AF-TENG consists of two copper layer and a membrane in a cuboid acrylic channel. The effect of membrane materials, including fluorinated ethylene propylene (FEP), polytetrafluoroethylene (PTFE) and Kapton, length of membrane, inlet velocity and humidity on the performance of AF-TENG have been systematically investigated. As wind flows through a designed channel, the fluttering of the membrane, which leads to its contact and separation between the top

and bottom copper surfaces. The membrane moving up and down periodically driven by wind flow can result in periodical electrical output signals (voltage, current, charge) of the AF-TENG. The corresponding frequency of the AF-TENG signal is found to increase in a linear relationship with the wind speed and not effected by hysteresis effect, showing that it can serve as an wind speed sensor. Interestingly, as environmental humidity increases, the amplitude of voltage and current output of the AF-TENG deceases dramatically, while the fluttering frequency of the output remains the same due to high humidity can decrease the charge density in the membrane surface but have no effect on the fluttering motion of the membrane. The real-time wind speed measured through analyzing frequency of the voltage of the AF-TENG agrees well with a commercial wind speed, and the corresponding speed sensitivity is about 0.13(m/s)/Hz or 7.7Hz/(m/s). Therefore, the fabricated self-powered AF-TENG has shown potential applications in wireless environmental monitoring networks, even in high humidity environment.

Author information

Corresponding Author: zhong.wang@mse.gatech.edu
Author Contributions: §: X. M.Y., Y.-C. W. and S. L. Z. contributed equally to this work.
Notes: The authors declare no competing financial interest.

Acknowledgments

This work was supported by the National Key Research and Development Program of China (No. 2016YFA0202704), the National Natural Science Foundation of China (No. 51506019, 51432005, 5151101243, 51561145021), the Fundamental Research Funds for the Central Universities, China (Nos. 3132016337, 3132016204).

References

1. Lee, S., et al., *Super - Flexible Nanogenerator for Energy Harvesting from Gentle Wind and as an Active Deformation Sensor.* Advanced Functional Materials, 2013. **23**(19): p. 2445-2449.
2. Zhang, R., et al., *Nanogenerator as an active sensor for vortex capture and ambient wind-velocity detection.* Energy & Environmental Science, 2012. **5**(9): p. 8528-8533.
3. Wang, Z.L., *On Maxwell's displacement current for energy and sensors: the origin of nanogenerators.* Materials Today, 2017.
4. Wang, Z.L., et al., *Triboelectric Nanogenerators*. Green Energy and Technology. 2016: Springer.
5. Wang, Z., J. Chen, and L. Lin, *Progress in triboelectric nanogenerators as a new energy technology and self-powered sensors.* Energy & Environmental Science, 2015. **8**(8): p. 2250-2282.
6. Zi, Y. and Z.L. Wang, *Nanogenerators: An emerging technology towards nanoenergy.* APL

Materials, 2017. **5**(7): p. 074103.

7. Bae, J., et al., *Flutter-driven triboelectrification for harvesting wind energy.* Nature Communications, 2014. **5**: p. 4929.
8. Wang, Z., *Triboelectric nanogenerators as new energy technology and self-powered sensors – Principles, problems and perspectives.* Faraday Discussions, 2015. **176**(0): p. 447-458.
9. Zi, Y., et al., *Harvesting Low-Frequency (< 5 Hz) Irregular Mechanical Energy: A Possible Killer Application of Triboelectric Nanogenerator.* ACS nano, 2016. **10**(4): p. 4797-4805.
10. Cao, X., et al., *Triboelectric Nanogenerators Driven Self‐Powered Electrochemical Processes for Energy and Environmental Science.* Advanced Energy Materials, 2016.
11. Zheng, Q., et al., *Robust Multilayered Encapsulation for High-Performance Triboelectric Nanogenerator in Harsh Environment.* ACS Applied Materials & Interfaces, 2016.
12. Ahmed, A., et al., *A washable, stretchable, and self-powered human-machine interfacing Triboelectric nanogenerator for wireless communications and soft robotics pressure sensor arrays.* Extreme Mechanics Letters, 2017. **13**: p. 25-35.
13. Luo, J., et al., *Ultrasensitive self-powered pressure sensing system.* Extreme Mechanics Letters, 2015. **2**: p. 28-36.
14. Li, D., et al., *Energy harvesting by means of flow-induced vibrations on aerospace vehicles.* Progress in Aerospace Sciences, 2016.
15. Nabavi, S. and L. Zhang, *Portable Wind Energy Harvesters for Low-Power Applications: A Survey.* Sensors, 2016. **16**(7): p. 1101.
16. Zhao, Z., et al., *Freestanding Flag-Type Triboelectric Nanogenerator for Harvesting High-Altitude Wind Energy from Arbitrary Directions.* ACS nano, 2016. **10**(2): p. 1780-1787.
17. Su, Y., et al., *Wind energy harvesting and self-powered flow rate sensor enabled by contact electrification.* Journal of Physics D: Applied Physics, 2016. **49**(21): p. 215601.
18. Quan, Z., et al., *Robust Thin Films‐Based Triboelectric Nanogenerator Arrays for Harvesting Bidirectional Wind Energy.* Advanced Energy Materials, 2016. **6**(5).
19. Phan, H., et al., *Aerodynamic and aeroelastic flutters driven triboelectric nanogenerators for harvesting broadband airflow energy.* Nano Energy, 2017. **33**: p. 476-484.
20. Yang, Y., et al., *Triboelectric nanogenerator for harvesting wind energy and as self-powered wind vector sensor system.* ACS nano, 2013. **7**(10): p. 9461-9468.
21. Wang, J., et al., *Smart network node based on hybrid nanogenerator for self-powered multifunctional sensing.* Nano Energy, 2017. **33**: p. 418-426.
22. Wang, S., et al., *Elasto-Aerodynamics-Driven Triboelectric Nanogenerator for Scavenging Air-Flow Energy.* ACS nano, 2015. **9**(10): p. 9554-9563.
23. Perez, M., et al., *An electret-based aeroelastic flutter energy harvester.* Smart Materials and Structures, 2015. **24**(3): p. 035004.
24. Archer, C.L. and M.Z. Jacobson, *Evaluation of global wind power.* Journal of Geophysical Research: Atmospheres, 2005. **110**(D12): p. n/a-n/a.
25. Seol, M.-L., et al., *Hysteretic behavior of contact force response in triboelectric nanogenerator.* Nano Energy, 2017. **32**: p. 408-413.
26. Su, Z., et al., *Asymmetrical Triboelectric Nanogenerator with Controllable Direct Electrostatic Discharge.* Advanced Functional Materials, 2016.
27. Argentina, M. and L. Mahadevan, *Fluid-flow-induced flutter of a flag.* Proceedings of the National academy of Sciences of the United States of America, 2005. **102**(6): p. 1829-1834.

28. Lee, J.H., W.-X. Huang, and H.J. Sung, *Flapping dynamics of a flexible flag in a uniform flow.* Fluid Dynamics Research, 2014. **46**(5): p. 055517.
29. Shelley, M.J. and J. Zhang, *Flapping and bending bodies interacting with fluid flows.* Annual Review of Fluid Mechanics, 2011. **43**: p. 449-465.
30. Huang, W.-X. and H.J. Sung, *Three-dimensional simulation of a flapping flag in a uniform flow.* Journal of Fluid Mechanics, 2010. **653**: p. 301-336.
31. Taneda, S., *Waving motions of flags.* Journal of the Physical Society of Japan, 1968. **24**(2): p. 392-401.
32. Zhang, J., et al., *Flexible filaments in a flowing soap film as a model for one-dimensional flags in a two-dimensional wind.* Nature, 2000. **408**(6814): p. 835-839.
33. Shelley, M., N. Vandenberghe, and J. Zhang, *Heavy flags undergo spontaneous oscillations in flowing water.* Physical review letters, 2005. **94**(9): p. 094302.
34. Virot, E., X. Amandolese, and P. Hémon, *Fluttering flags: An experimental study of fluid forces.* Journal of Fluids and Structures, 2013. **43**: p. 385-401.
35. Allen, J. and A. Smits, *Energy harvesting eel.* Journal of fluids and structures, 2001. **15**(3-4): p. 629-640.
36. Eloy, C., et al., *Aeroelastic instability of cantilevered flexible plates in uniform flow.* Journal of Fluid Mechanics, 2008. **611**: p. 97-106.
37. Landau, L.D. and E. Lifshitz, *Theory of Elasticity, vol. 7.* Course of Theoretical Physics, 1986. **3**: p. 109.
38. Xie, Y., et al., *Grating-Structured Freestanding Triboelectric-Layer Nanogenerator for Harvesting Mechanical Energy at 85% Total Conversion Efficiency.* Advanced Materials, 2014. **26**(38): p. 6599-6607.
39. Yu, H., et al., *A Self-Powered Dynamic Displacement Monitoring System Based on Triboelectric Accelerometer.* Advanced Energy Materials, 2017: p. 1700565-n/a.
40. Niu, S., et al., *Theoretical Investigation and Structural Optimization of Single-Electrode Triboelectric Nanogenerators.* Advanced Functional Materials, 2014. **24**(22): p. 3332-3340.
41. Lin, L., et al., *Triboelectric Active Sensor Array for Self-Powered Static and Dynamic Pressure Detection and Tactile Imaging.* ACS Nano, 2013. **7**(9): p. 8266-8274.
42. Williamson, C.H., *Vortex dynamics in the cylinder wake.* Annual review of fluid mechanics, 1996. **28**(1): p. 477-539.